Biomedical Optics EXPRESS

Differentiation of *ex vivo* human breast tissue using polarization-sensitive optical coherence tomography

Fredrick A. South,[1,2] Eric J. Chaney,[1] Marina Marjanovic,[1] Steven G. Adie,[1] and Stephen A. Boppart[1,2,3,4,*]

[1]*Beckman Institute for Advanced Science and Technology, 405 N Mathews Avenue, Urbana, IL 61801, USA*
[2]*Department of Electrical and Computer Engineering, 306 N Wright Street, Urbana, IL 61801, USA*
[3]*Department of Bioengineering, 1304 W Springfield Avenue, Urbana, IL 61801, USA*
[4]*Department of Internal Medicine, 506 S Mathews Avenue, Urbana, IL 61801, USA*
[*]*boppart@illinois.edu*

Abstract: Successful treatment of breast cancer typically requires surgical removal of the tumor. Optical coherence tomography (OCT) has been previously developed for real-time imaging of the surgical margin. However, it can be difficult to distinguish between normal stromal tissue and cancer tissue based on scattering intensity and structure alone. Polarization-sensitive optical coherence tomography (PS-OCT) is sensitive to form birefringence of biological tissue. We report on the development of a high-speed PS-OCT system and imaging of *ex vivo* human breast tissue, showing enhanced contrast between healthy and cancerous tissues based upon collagen content confirmed with corresponding histology. These results demonstrate the feasibility of using PS-OCT to supplement structural OCT as a possible method for intraoperative tumor margin evaluation.

OCIS codes: (110.4500) Optical coherence tomography; (170.4500) Optical coherence tomography; (170.3880) Medical and biological imaging; (260.1440) Birefringence; (110.5405) Polarimetric imaging; (170.6935) Tissue characterization.

References and links

1. American Cancer Society, *Breast Cancer Facts & Figs. 2013–2014* (American Cancer Society, Atlanta, GA, 2013).
2. B. Fisher, S. Anderson, J. Bryant, R. G. Margolese, M. Deutsch, E. R. Fisher, J.-H. Jeong, and N. Wolmark, "Twenty-year follow-up of a randomized trial comparing total mastectomy, lumpectomy, and lumpectomy plus irradiation for the treatment of invasive breast cancer," N. Engl. J. Med. **347**(16), 1233–1241 (2002).
3. U. Veronesi, N. Cascinelli, L. Mariani, M. Greco, R. Saccozzi, A. Luini, M. Aguilar, and E. Marubini, "Twenty-year follow-up of a randomized study comparing breast-conserving surgery with radical mastectomy for early breast cancer," N. Engl. J. Med. **347**(16), 1227–1232 (2002).
4. P. Ananthakrishnan, F. L. Balci, and J. P. Crowe, "Optimizing surgical margins in breast conservation," Int. J. Surg. Oncol. **2012**, 585670 (2012).
5. M. F. Dillon, A. D. K. Hill, C. M. Quinn, E. W. McDermott, and N. O'Higgins, "A pathologic assessment of adequate margin status in breast-conserving therapy," Ann. Surg. Oncol. **13**(3), 333–339 (2006).
6. A. Luini, J. Rososchansky, G. Gatti, S. Zurrida, P. Caldarella, G. Viale, G. Rosali dos Santos, and A. Frasson, "The surgical margin status after breast-conserving surgery: Discussion of an open issue," Breast Cancer Res. Treat. **113**(2), 397–402 (2009).
7. G. P. Swanson, K. Rynearson, and R. Symmonds, "Significance of margins of excision on breast cancer recurrence," Am. J. Clin. Oncol. **25**(5), 438–441 (2002).
8. M. Azu, P. Abrahamse, S. J. Katz, R. Jagsi, and M. Morrow, "What is an adequate margin for breast-conserving surgery? Surgeon attitudes and correlates," Ann. Surg. Oncol. **17**(2), 558–563 (2010).
9. A. Taghian, M. Mohiuddin, R. Jagsi, S. Goldberg, E. Ceilley, and S. Powell, "Current perceptions regarding surgical margin status after breast-conserving therapy: results of a survey," Ann. Surg. **241**(4), 629–639 (2005).
10. C. Kotwall, M. Ranson, A. Stiles, and M. S. Hamann, "Relationship between initial margin status for invasive breast cancer and residual carcinoma after re-excision," Am. Surg. **73**(4), 337–343 (2007).
11. J. F. Waljee, E. S. Hu, L. A. Newman, and A. K. Alderman, "Predictors of re-excision among women undergoing breast-conserving surgery for cancer," Ann. Surg. Oncol. **15**(5), 1297–1303 (2008).

#214173 - $15.00 USD Received 16 Jun 2014; revised 23 Aug 2014; accepted 27 Aug 2014; published 4 Sep 2014

12. T. S. Menes, P. I. Tartter, I. Bleiweiss, J. H. Godbold, A. Estabrook, and S. R. Smith, "The consequence of multiple re-excisions to obtain clear lumpectomy margins in breast cancer patients," Ann. Surg. Oncol. **12**(11), 881–885 (2005).
13. M. Morrow, R. Jagsi, A. K. Alderman, J. J. Griggs, S. T. Hawley, A. S. Hamilton, J. J. Graff, and S. J. Katz, "Surgeon recommendations and receipt of mastectomy for treatment of breast cancer," JAMA **302**(14), 1551–1556 (2009).
14. T. P. Olson, J. Harter, A. Muñoz, D. M. Mahvi, and T. M. Breslin, "Frozen section analysis for intraoperative margin assessment during breast-conserving surgery results in low rates of re-excision and local recurrence," Ann. Surg. Oncol. **14**(10), 2953–2960 (2007).
15. E. K. Valdes, S. K. Boolbol, J.-M. Cohen, and S. M. Feldman, "Intra-operative touch preparation cytology; Does it have a role in re-excision lumpectomy?" Ann. Surg. Oncol. **14**(3), 1045–1050 (2007).
16. B. J. Vakoc, D. Fukumura, R. K. Jain, and B. E. Bouma, "Cancer imaging by optical coherence tomography: Preclinical progress and clinical potential," Nat. Rev. Cancer **12**(5), 363–368 (2012).
17. S. A. Boppart, W. Luo, D. L. Marks, and K. W. Singletary, "Optical coherence tomography: Feasibility for basic research and image-guided surgery of breast cancer," Breast Cancer Res. Treat. **84**(2), 85–97 (2004).
18. D. Savastru, E. W. Chang, S. Miclos, M. B. Pitman, A. Patel, and N. Iftimia, "Detection of breast surgical margins with optical coherence tomography imaging: A concept evaluation study," J. Biomed. Opt. **19**(5), 056001 (2014).
19. P. L. Hsiung, D. R. Phatak, Y. Chen, A. D. Aguirre, J. G. Fujimoto, and J. L. Connolly, "Benign and malignant lesions in the human breast depicted with ultrahigh resolution and three-dimensional optical coherence tomography," Radiology **244**(3), 865–874 (2007).
20. C. Zhou, D. W. Cohen, Y. H. Wang, H. C. Lee, A. E. Mondelblatt, T. H. Tsai, A. D. Aguirre, J. G. Fujimoto, and J. L. Connolly, "Integrated optical coherence tomography and microscopy for *ex vivo* multiscale evaluation of human breast tissues," Cancer Res. **70**(24), 10071–10079 (2010).
21. F. T. Nguyen, A. M. Zysk, E. J. Chaney, J. G. Kotynek, U. J. Oliphant, F. J. Bellafiore, K. M. Rowland, P. A. Johnson, and S. A. Boppart, "Intraoperative evaluation of breast tumor margins with optical coherence tomography," Cancer Res. **69**(22), 8790–8796 (2009).
22. F. South, M. Marjanovic, S. G. Adie, E. J. Chaney, P. Ray, K. Cradock, J. Brockenbrough, G. Liu, G. Monroy, R. Nolan, N. D. Shemonski, J. Putney, D. Darga, A. Cittadine, P. S. Carney, and S. A. Boppart, "Intraoperative hand-held probe-based imaging of *in situ* breast tumor margins and lymph nodes using OCT and ISAM," presented at SPIE Photonics West BIOS, San Francisco, CA, 3 Feb. 2013.
23. S. J. Erickson-Bhatt, R. Nolan, N. D. Shemonski, S. G. Adie, J. Putney, D. Darga, D. T. McCormick, A. Cittadine, M. Marjanovic, E. J. Chaney, G. L. Monroy, F. South, P. S. Carney, K. A. Cradock, Z. G. Liu, P. S. Ray, and S. A. Boppart, "*In vivo* intra-operative breast tumor margin detection using a portable OCT system with a handheld surgical imaging probe," Proc. SPIE **89351**, 89351C (2014).
24. O. Assayag, M. Antoine, B. Sigal-Zafrani, M. Riben, F. Harms, A. Burcheri, K. Grieve, E. Dalimier, B. Le Conte de Poly, and C. Boccara, "Large field, high resolution full-field optical coherence tomography: A pre-clinical study of human breast tissue and cancer assessment," Technol. Cancer Res. Treat. **13**(5), 455–468 (2014).
25. R. A. McLaughlin, B. C. Quirk, A. Curatolo, R. W. Kirk, L. Scolaro, D. Lorenser, P. D. Robbins, B. A. Wood, C. M. Saunders, and D. D. Sampson, "Imaging of breast cancer with optical coherence tomography needle probes: Feasibility and initial results," IEEE J. Sel. Top. Quantum Electron. **18**(3), 1184–1191 (2012).
26. A. M. Zysk, F. T. Nguyen, E. J. Chaney, J. G. Kotynek, U. J. Oliphant, F. J. Bellafiore, P. A. Johnson, K. M. Rowland, and S. A. Boppart, "Clinical feasibility of microscopically-guided breast needle biopsy using a fiber-optic probe with computer-aided detection," Technol. Cancer Res. Treat. **8**(5), 315–321 (2009).
27. W. C. Kuo, J. Kim, N. D. Shemonski, E. J. Chaney, D. R. Spillman, Jr., and S. A. Boppart, "Real-time three-dimensional optical coherence tomography image-guided core-needle biopsy system," Biomed. Opt. Express **3**(6), 1149–1161 (2012).
28. A. M. Zysk, E. J. Chaney, and S. A. Boppart, "Refractive index of carcinogen-induced rat mammary tumours," Phys. Med. Biol. **51**(9), 2165–2177 (2006).
29. J. F. de Boer, T. E. Milner, M. J. C. van Gemert, and J. S. Nelson, "Two-dimensional birefringence imaging in biological tissue by polarization-sensitive optical coherence tomography," Opt. Lett. **22**(12), 934–936 (1997).
30. J. F. de Boer and T. E. Milner, "Review of polarization sensitive optical coherence tomography and Stokes vector determination," J. Biomed. Opt. **7**(3), 359–371 (2002).
31. M. R. Hee, D. Huang, E. A. Swanson, and J. G. Fujimoto, "Polarization-sensitive low-coherence reflectometer for birefringence characterization and ranging," J. Opt. Soc. Am. B **9**(6), 903–908 (1992).
32. M. Born and E. Wolf, *Principles of Optics: Electromagnetic Theory of Propagation, Interference and Diffraction of Light*, 7th ed. (Cambridge University Press, Cambridge, UK, 1999), pp. 837–840.
33. J. J. Pasquesi, S. C. Schlachter, M. D. Boppart, E. Chaney, S. J. Kaufman, and S. A. Boppart, "*In vivo* detection of exercised-induced ultrastructural changes in genetically-altered murine skeletal muscle using polarization-sensitive optical coherence tomography," Opt. Express **14**(4), 1547–1556 (2006).
34. S. K. Nadkarni, M. C. Pierce, B. H. Park, J. F. de Boer, P. Whittaker, B. E. Bouma, J. E. Bressner, E. Halpern, S. L. Houser, and G. J. Tearney, "Measurement of collagen and smooth muscle cell content in atherosclerotic plaques using polarization-sensitive optical coherence tomography," J. Am. Coll. Cardiol. **49**(13), 1474–1481 (2007).
35. J. Strasswimmer, M. C. Pierce, B. H. Park, V. Neel, and J. F. de Boer, "Polarization-sensitive optical coherence tomography of invasive basal cell carcinoma," J. Biomed. Opt. **9**(2), 292–298 (2004).

#214173 - $15.00 USD Received 16 Jun 2014; revised 23 Aug 2014; accepted 27 Aug 2014; published 4 Sep 2014

36. Y. Verma, M. Gautam, K. D. Rao, M. K. Swami, and P. K. Gupta, "Imaging of human breast tissue using polarization sensitive optical coherence tomography," Laser Phys. **21**(12), 2143–2148 (2011).
37. R. Greenberg, Y. Skornick, and O. Kaplan, "Management of breast fibroadenomas," J. Gen. Intern. Med. **13**(9), 640–645 (1998).
38. S. G. Adie, T. R. Hillman, and D. D. Sampson, "Detection of multiple scattering in optical coherence tomography using the spatial distribution of Stokes vectors," Opt. Express **15**(26), 18033–18049 (2007).
39. R. Huber, M. Wojtkowski, and J. G. Fujimoto, "Fourier domain mode locking (FDML): A new laser operating regime and applications for optical coherence tomography," Opt. Express **14**(8), 3225–3237 (2006).
40. R. Huber, D. C. Adler, and J. G. Fujimoto, "Buffered Fourier domain mode locking: Unidirectional swept laser sources for optical coherence tomography imaging at 370,000 lines/s," Opt. Lett. **31**(20), 2975–2977 (2006).
41. H. C. Hendargo, R. P. McNabb, A.-H. Dhalla, N. Shepherd, and J. A. Izatt, "Doppler velocity detection limitations in spectrometer-based versus swept-source optical coherence tomography," Biomed. Opt. Express **2**(8), 2175–2188 (2011).
42. S. L. Jiao, W. R. Yu, G. Stoica, and L. V. Wang, "Optical-fiber-based Mueller optical coherence tomography," Opt. Lett. **28**(14), 1206–1208 (2003).
43. G. J. Liu, J. Zhang, L. F. Yu, T. Q. Xie, and Z. P. Chen, "Real-time polarization-sensitive optical coherence tomography data processing with parallel computing," Appl. Opt. **48**(32), 6365–6370 (2009).
44. B. Young and J. W. Heath, *Wheater's Functional Histology*, 4th ed. (Churchill Livingstone, New York, 2000).
45. M. W. Conklin, J. C. Eickhoff, K. M. Riching, C. A. Pehlke, K. W. Eliceiri, P. P. Provenzano, A. Friedl, and P. J. Keely, "Aligned collagen is a prognostic signature for survival in human breast carcinoma," Am. J. Pathol. **178**(3), 1221–1232 (2011).
46. P. P. Provenzano, D. R. Inman, K. W. Eliceiri, J. G. Knittel, L. Yan, C. T. Rueden, J. G. White, and P. J. Keely, "Collagen density promotes mammary tumor initiation and progression," BMC Med. **6**(1), 11 (2008).
47. A. Trentham-Dietz, R. E. Gangnon, B. L. Sprague, K. W. Eliceiri, J. S. Bredfeldt, N. Surachaicharn, P. J. Campagnola, A. Friedl, P. A. Newcomb, and P. J. Keely, "Alteration of stromal collagen fiber orientation in DCIS," presented at *San Antonio Breast Cancer Symposium*, San Antonio, TX, 10–14 Dec. 2013.

1. Introduction

Breast cancer is the second leading cause of cancer death among women, behind lung cancer [1]. The current standard of care is breast-conserving surgery, which has been shown to be equivalent to mastectomy [2, 3]. It is important that the surgical margin is clear of cancer tissue to prevent immediate reoperation and reduce the risk for local recurrence. There is much debate in the literature regarding margin size [4–7], however, over 50% of surveyed surgeons consider no tumor present within 1-2 mm of the surface to be sufficient for a clear margin [8, 9]. As 30% to 60% of patients undergo reexcision, there remains a significant need for a real-time evaluation of the tumor margin [10–13]. Unfortunately, existing methods for intraoperative tumor margin evaluation are limited and considered inadequate. Frozen section provides poor results due to difficulties sectioning adipose tissue, and adds 25-35 minutes to operating room time [14]. Touch prep cytology provides rapid assessment, but is limited to evaluating cells on the immediate surface of the tissue [15].

Over the past decade, optical coherence tomography (OCT) has been developed for applications in cancer imaging [16]. The combination of optical resolution, high-speed, and millimeter scale imaging depth makes OCT well suited for surgical margin evaluation. Several pilot studies have explored the application of OCT to breast cancer imaging, including preclinical animal studies [17, 18], human tissue imaging [19, 20], and intraoperative imaging [21]. Currently a handheld OCT probe is being evaluated for *in vivo* margin assessment which allows tissue within the surgical cavity to be imaged prior to resection [22, 23]. Other OCT techniques can also be used for breast imaging, including full-field OCT for margin assessment [24], and OCT needle probes for biopsy assessment [25–27]. These previous studies have shown that breast cancer appears more highly scattering than healthy tissue and disrupts the normal structure of adipose and stroma found in the breast. However, solid invasive tumors may be difficult to distinguish from islands of fibrous stromal tissue [19, 28]. This may be due to a lack of clear structures and similar refractive indices [28].

Polarization-sensitive optical coherence tomography (PS-OCT) is a variant of OCT that measures the polarization state of backscattered light [29–31]. Anisotropic biological tissues such as collagen fibers exhibit form birefringence, causing the polarization to change as light propagates through the tissue [32]. Although these fibers are not individually resolved in PS-OCT, the collagen content can be inferred through the observed birefringence. This allows

#214173 - $15.00 USD Received 16 Jun 2014; revised 23 Aug 2014; accepted 27 Aug 2014; published 4 Sep 2014

PS-OCT to probe the sub-resolution microenvironment while maintaining the imaging depth and field-of-view of OCT. Microstructural changes have been observed with PS-OCT in applications such as muscular dystrophy, collagenous plaques, and skin cancer [33–35]. The difference in collagen content between the stromal and tumor tissues could be used as an additional source of contrast for breast cancer imaging. PS-OCT has previously been used to distinguish between benign fibroadenoma and malignant invasive ductal carcinoma [36]. However, fibroadenoma is rarely excised due to the benign nature of the tumor [37]. It remains a significant challenge to distinguish between the fibrous tissue that is regularly encountered and invasive tumor.

2. Methods

2.1 Polarization-sensitive OCT system

The PS-OCT system presented in this paper is based upon the design by Adie, et al. previously published in [38]. This design has previously been shown to be sensitive to changes in polarization-state in both phantom and tissue imaging. The modified design presented here has several improvements over the previous design including circularly polarized sample illumination light, dual-balanced Fourier domain detection, and improved imaging speed.

The swept-source PS-OCT system developed for this study is shown in Fig. 1. The laser source is a Fourier domain mode locking (FDML) laser with a center wavelength of 1310 nm, a 3 dB bandwidth of 122.5 nm, and a double-buffered A-line rate of 236.5 kHz [39, 40]. A small portion of the laser light is directed to a fixed path length Mach-Zehnder interferometer for calibrating the spectrum resampling parameters, and to a fiber Bragg grating used for generating the A-line trigger [41].

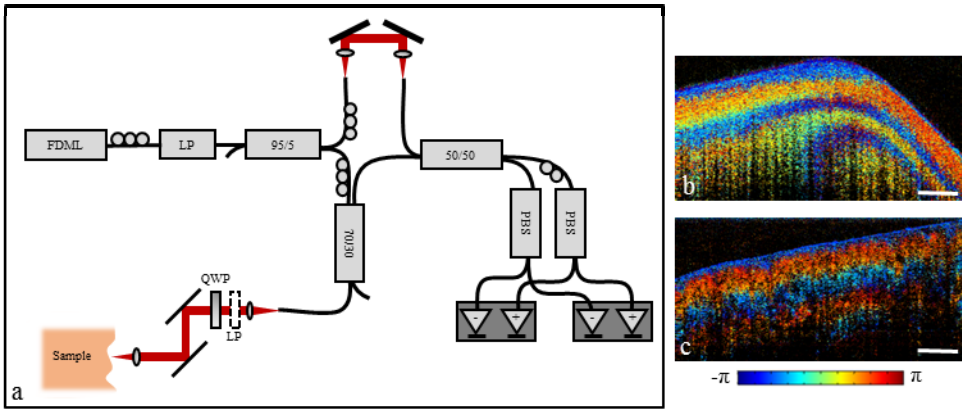

Fig. 1. (a) Swept-source PS-OCT system design. FDML: Fourier domain mode-locked laser; LP: Linear polarizer; PBS: Polarizing beam splitter; QWP: Quarter-wave plate. (b) PS-OCT image of molded plastic. (c) PS-OCT image of chicken breast muscle. Scale bar represents 500 μm.

The polarization-sensitive interferometer was built using single-mode SMF-28 fiber and was calibrated at the beginning of each imaging session. Control over the polarization state was achieved using a combination of polarization paddles and polarization optics. Light from the FDML laser was passed through a fiber polarizer into a Mach-Zehnder interferometer. The reference arm light was balanced between two orthogonal polarization channels using the polarization paddles. To maximize interaction with tissue birefringence, the sample arm light was chosen to be circularly polarized [30]. This required that light exiting the sample arm fiber be linearly polarized at 45° with respect to the quarter-wave plate axis. This condition was achieved by temporarily removing the quarter-wave plate and inserting a linear polarizer into the sample arm at the correct orientation. Light exiting the sample arm fiber was adjusted

#214173 - $15.00 USD Received 16 Jun 2014; revised 23 Aug 2014; accepted 27 Aug 2014; published 4 Sep 2014

to align with the polarizer. The polarizer was then removed and the quarter-wave plate replaced for PS-OCT imaging. The resulting interference pattern was measured using polarization diverse dual-balanced detection. The full-width half-maximum (FWHM) transverse resolution was 9 μm, and the FWHM axial resolution was 9.9 μm in air, or 7 μm in tissue.

As in the previous work by Adie et. al, the OCT intensity image I was calculated as the total intensity of the two output channels

$$I = \left|E_{out,1}\right|^2 + \left|E_{out,2}\right|^2, \tag{1}$$

while the PS-OCT signal, here denoted as P, was calculated as the phase difference between the two channels

$$P = Arg\left(E_{out,1} \times E_{out,2}^*\right), \tag{2}$$

where "*" denotes the complex conjugate. This resulted in a measurement range of [-π π] which does not represent the actual phase retardation, but the phase difference between the detection channels. This calculation represents a qualitative assessment of change in polarization state, as described below.

Following calibration, the sample arm input light was circularly polarized and described by the Jones vector

$$\mathbf{E}_{in} = \begin{bmatrix} 1 \\ i \end{bmatrix} \frac{1}{\sqrt{2}}. \tag{3}$$

Light then reflected from within the sample and returned through the quarter-wave plate, exiting the free-space portion of the sample arm with polarization state given by

$$\mathbf{E}_{sample} = \mathbf{QWP}_{45^\circ}\, \mathbf{J}_{sample}\, \mathbf{E}_{in}, \tag{4}$$

where $\mathbf{QWP}_{45^\circ}$ indicates the Jones matrix of the sample arm quarter-wave plate, and $\mathbf{J}_{sample}$ indicates the round-trip Jones matrix of the sample itself. This resulted in the standard free-space PS-OCT measurement, first given by Hee, et al. [31], which enables direct calculation of both cumulative phase-retardation and optic axis.

In our system, light returning from the sample arm was further modified by the single-mode fiber resulting in

$$\mathbf{E}_{out} = \mathbf{J}_{fiber}\mathbf{E}_{sample}, \tag{5}$$

where the fiber is represented by the Jones matrix $\mathbf{J}_{fiber}$. The single-mode fiber can be modeled as an elliptical retarder [42]. The phase retardation, ellipticity, and optic axis of the single-mode fiber are generally unknown, greatly complicating direct recovery of the sample birefringence. However, for a fiber with an optic axis that does not equal zero or π/2, the phase difference between the two polarization channels becomes a non-constant function of sample birefringence. Under this assumption, the calculation presented in Eq. (5) results in a qualitative measurement of cumulative phase retardation and can be used to identify the presence of birefringence.

Although the resulting polarization-sensitive images are qualitative in nature, they are still effective at visualizing the presence of sample birefringence. This is demonstrated in Figs. 1(b) and 1(c) which show polarization-sensitive images of a molded plastic phantom and chicken breast muscle, respectively. In addition, this design allows for the use of single-mode fiber without polarization-modulation, improving the imaging speed by a factor of two over traditional single-mode fiber PS-OCT designs.

#214173 - $15.00 USD Received 16 Jun 2014; revised 23 Aug 2014; accepted 27 Aug 2014; published 4 Sep 2014

2.2 Data acquisition, processing, and display

The two PS-OCT detection channels were digitized at 250 MS/s each using a high-speed digitizer (AlazarTech ATS9350), resulting in a total acquisition rate of 1 GB/s. Data was then passed from page-locked CPU memory to the GPU (NVidia GTX 285) where it was processed and displayed in real time. Parallel processing was performed using the NVidia CUDA toolkit. Interoperability between CUDA and OpenGL allowed for real-time display of either the OCT or PS-OCT calculation directly from the GPU without needing to first return data to the CPU. This achieved a processing and display rate of approximately 185,000 lines per second, which is an order of magnitude improvement over previously published PS-OCT results using CPU processing [43].

Due to the single-mode fiber design, PS-OCT measurements from different experiments may be circularly shifted along the measurement range with respect to one another, and therefore cover different regions of the color map. This made visual comparison of image sets somewhat difficult. To facilitate ease of comparison across imaging sets, the PS-OCT data was circularly shifted in post-processing, resulting in a measurement of $-\pi/2$ at the tissue surface for each data set. This caused the PS-OCT measurements to begin at the same location in the color map for each image, making comparison between image sets more intuitive.

For visualization in the *en face* plane, the average PS-OCT signal $\bar{P}$ was calculated along each A-line using the circular mean defined by

$$\bar{P} = Arg\left(\frac{1}{N}\sum_{n=1}^{N} e^{iP_n}\right), \tag{6}$$

where P_n is the PS-OCT measurement at depth pixel n, and N is the total number of depth pixels. This calculation assumes a constant optic axis throughout depth. The mean PS-OCT signal was then overlaid on the OCT average intensity projection. The OCT structural data was represented by the intensity, while the color indicated the mean PS-OCT signal. This allowed for simultaneous visualization of both reflectance and birefringence information in the *en face* dimension.

2.3 Tissue imaging

Excess human tissue not needed for clinical diagnosis was acquired from Carle Foundation Hospital in Urbana, Illinois under IRB protocols approved by both Carle Foundation Hospital and the University of Illinois at Urbana-Champaign. Breast tissue was received from 8 female mastectomy patients. All samples were transported on ice in saline, and were imaged *ex vivo* within 12 hours of initial surgical resection. Areas imaged with PS-OCT were marked with ink for histology correlation. Following formalin fixation, the tissue was processed for histological evaluation. Both H&E and picrosirius red staining were performed to determine disease type and collagen content, respectively.

3. Results

3.1 Fibro-adipose tissue

The breast is composed of a system of lobules and ducts suspended in adipose tissue. These lobular units are partitioned by a network of fibrous septa which is present throughout the breast [44]. The structural OCT image of normal fibro-adipose tissue is shown in Fig. 2(a), and the corresponding H&E histology is shown in Fig. 2(b). The adipocytes are recognizable in the OCT image due to their round shape and low scattering lipid interior, while the fibrous septa appear moderately scattering and are identified by a vein-like structure. However, in some cases it may be difficult to distinguish between these fibrous structures and a spiculated tumor invasion. The PS-OCT image in Fig. 2(c) illustrates change in polarization state due to propagation of light through the fibrous stroma. This suggests significant collagen content,

#214173 - $15.00 USD Received 16 Jun 2014; revised 23 Aug 2014; accepted 27 Aug 2014; published 4 Sep 2014

confirmed by the picrosirius red collagen stain in Fig. 2(d). The mean projection in Fig. 2(e) illustrates the OCT and PS-OCT information in the *en face* plane, where any change in color from the normalized value of $-\pi/2$ indicates significant birefringence. The birefringent network of fibrous stroma can be seen branching throughout the surrounding adipose tissue.

Stromal tissue can also take the form of relatively large patches or islands as shown in Fig. 3. It is this structure that is particularly difficult to distinguish from solid tumor. The OCT image is homogenously scattering without the branching pattern seen previously. However, the changes in polarization state seen in the PS-OCT image indicate a highly birefringent microstructure. This is confirmed by the dense collagen content seen in the histology. The *en face* projection shows birefringence throughout the tissue. Together, the normal tissues presented in Figs. 2 and 3 are representative of scenarios commonly encountered in intraoperative breast imaging.

3.3 Invasive ductal carcinoma

Invasive ductal carcinoma (IDC) occurs when cancer previously confined to the ductal system spreads into the surrounding tissue microenvironment. IDC may metastasize to the lymph nodes and throughout the body, and therefore complete surgical resection is imperative. IDC appears homogeneous and moderately scattering under OCT, as shown in Fig. 4(a). This is similar to the island of fibrous stroma shown previously in Fig. 3(a). However, the cellular composition is much different. Tumor cells have displaced the normal breast tissue, resulting in severe fragmentation of the collagen structures. This leads to low birefringence and a uniform polarization state in the PS-OCT image Fig. 4(c) (red arrow). An area of birefringence remains at the far right (green arrow) due to a circular bundle of collagen, indicating that not all of the fibrous tissue has been displaced or replaced. Figure 4(e) highlights the spread of the invasive cancer into the surrounding collagen matrix. This demonstrates the potential of PS-OCT to interrogate the tumor microenvironment, which is known to be an important factor in tumor growth [45, 46].

A more advanced invasion of ductal carcinoma is shown in Fig. 5. Once again, the IDC tissue structure is homogeneous and moderately scattering under traditional OCT. Yet the distinct contrast in birefringence seen in the PS-OCT image leads to improved differentiation of tissue type. In this case, there are very few collagen fibers remaining. Because of this, the polarization state remains unchanged throughout the vast majority of the data set.

3.2 Ductal carcinoma in situ

In ductal carcinoma *in situ* (DCIS) the cancer is still confined within the duct. Figure 6 demonstrates a case of cribriform type DCIS with grossly misshapen ducts clearly seen in the OCT structural image. While there may be a small change in collagen alignment at the disease boundary, the tumor remains inside the ductal system and therefore does not destroy the surrounding collagen structure [47]. Because of this, the surrounding collagen matrix remains quite birefringent. This can be seen in the PS-OCT image which shows birefringence throughout the surrounding tissue.

#214173 - $15.00 USD Received 16 Jun 2014; revised 23 Aug 2014; accepted 27 Aug 2014; published 4 Sep 2014

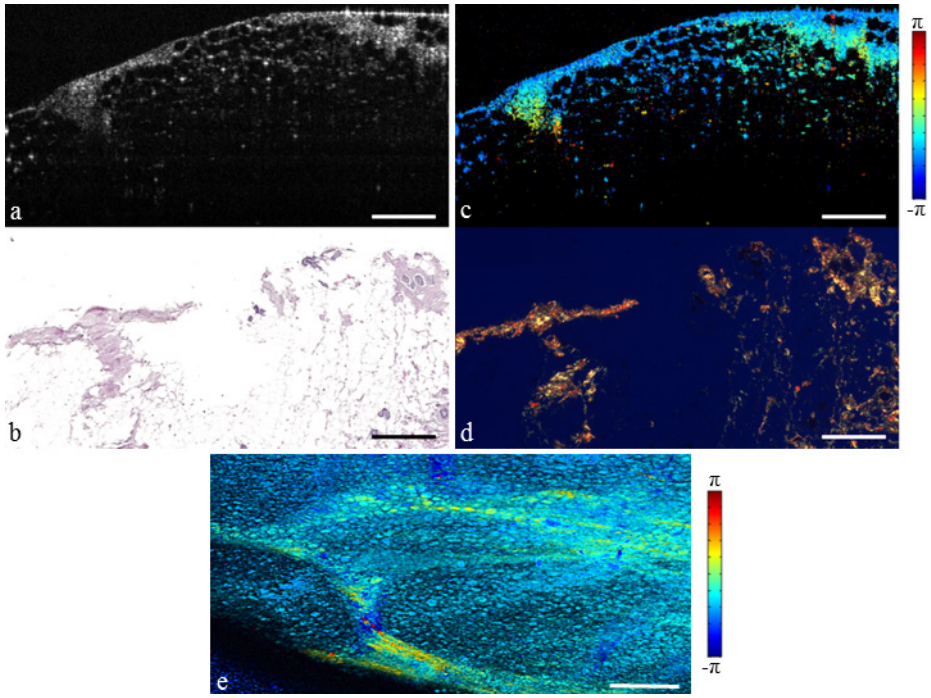

Fig. 2. Fibro-adipose human breast tissue. (a) Structural OCT image. (b) H&E-stained histology. (c) PS-OCT image (Media 1). (d) Picrosirius red stained histology. (e) *En face* PS-OCT projection. Scale bars represent 500 µm.

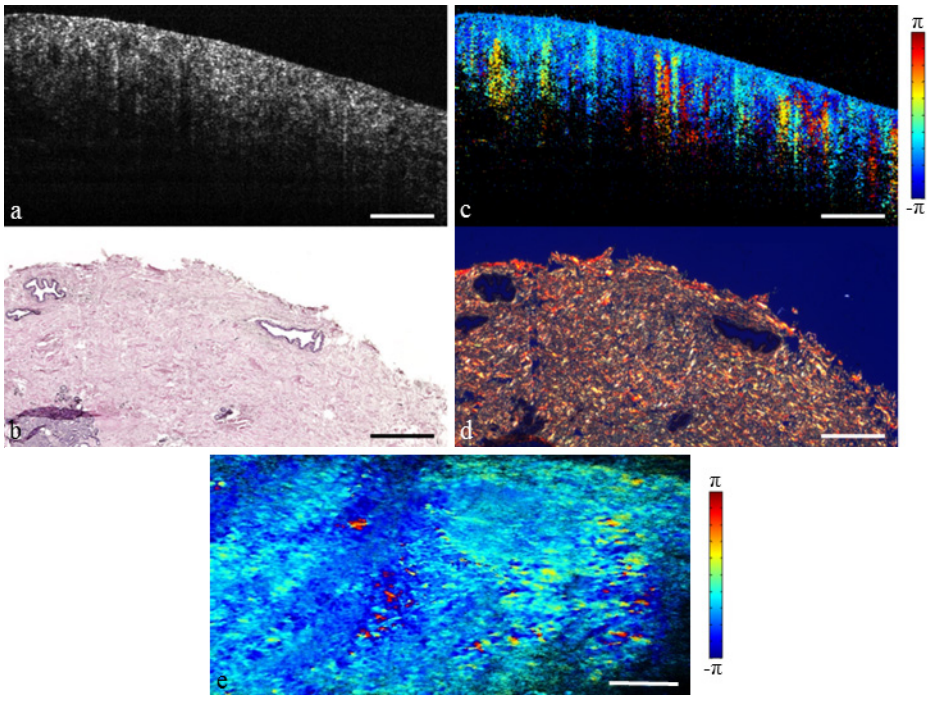

Fig. 3. Fibrous human breast tissue. (a) Structural OCT image. (b) H&E-stained histology. (c) PS-OCT image (Media 2). (d) Picrosirius red stained histology. (e) *En face* PS-OCT projection. Scale bars represent 500 µm.

#214173 - $15.00 USD Received 16 Jun 2014; revised 23 Aug 2014; accepted 27 Aug 2014; published 4 Sep 2014

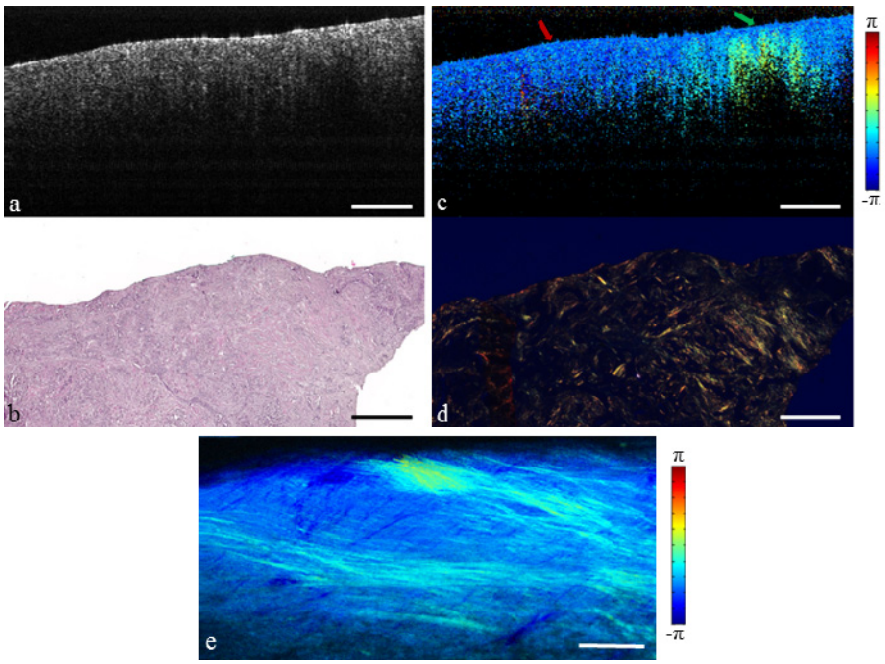

Fig. 4. Invasive ductal carcinoma replacing the surrounding fibrous environment. (a) Structural OCT image. (b) H&E-stained histology. (c) PS-OCT image (Media 3). Red arrow indicates tumor, green arrow indicates fibrous stroma. (d) Picrosirius red stained histology. (e) *En face* PS-OCT projection. Scale bars represent 500 µm.

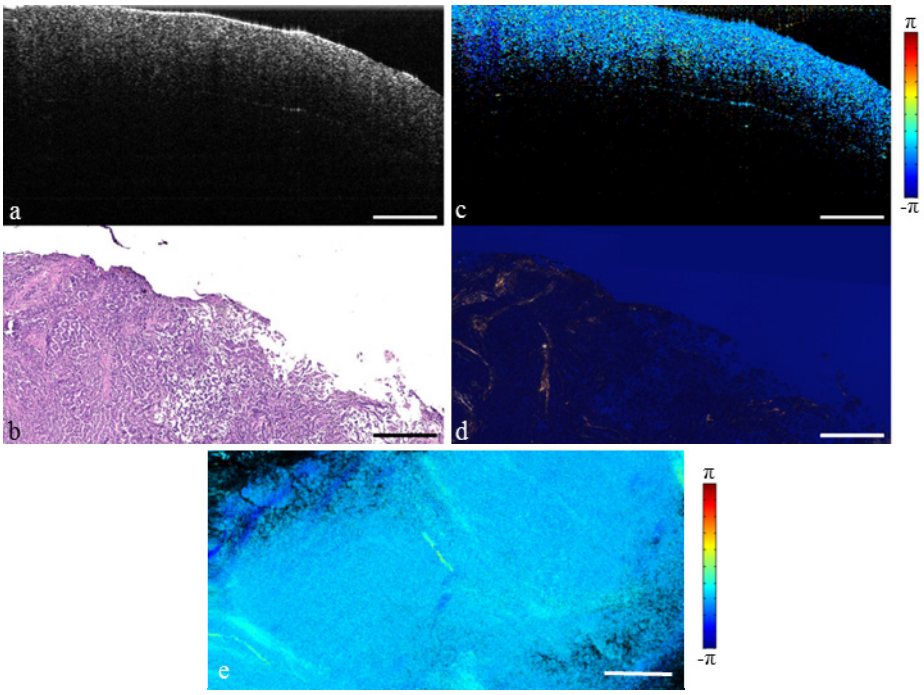

Fig. 5. Extensive invasive ductal carcinoma that has fully replaced normal breast tissue. (a) Structural OCT image. (b) H&E-stained histology. (c) PS-OCT image (Media 4). (d) Picrosirius red stained histology. (e) *En face* PS-OCT projection. Scale bars represent 500 µm.

#214173 - $15.00 USD Received 16 Jun 2014; revised 23 Aug 2014; accepted 27 Aug 2014; published 4 Sep 2014

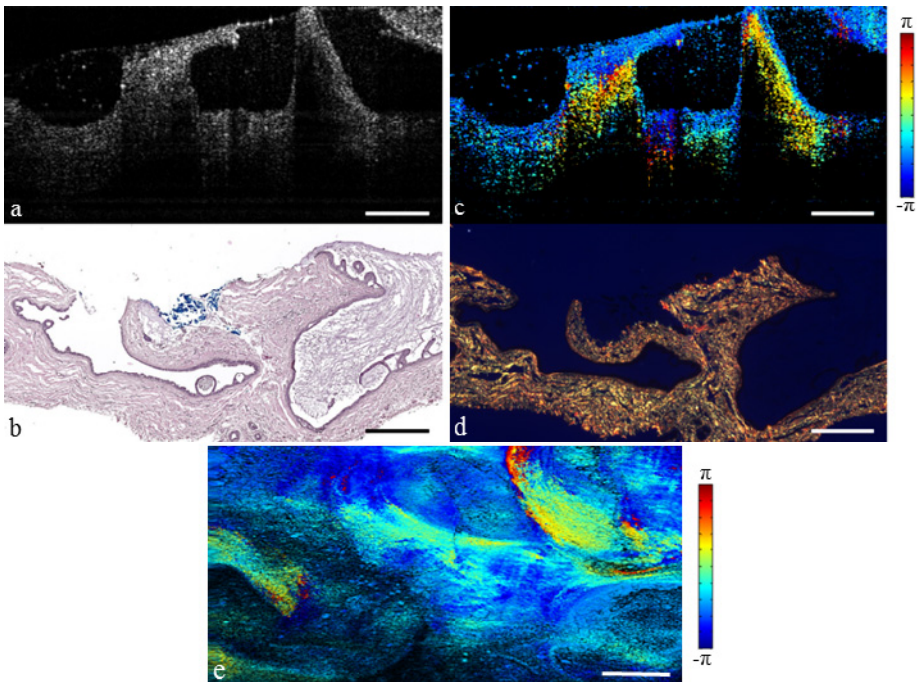

Fig. 6. Cribriform type ductal carcinoma *in situ*. (a) Structural OCT image. (b) H&E-stained histology. (c) PS-OCT image (Media 5). (d) Picrosirius red stained histology. (e) *En face* PS-OCT projection. Scale bars represent 500 μm.

4. Conclusion

The microstructural information provided by PS-OCT is shown to provide a significant enhancement in contrast between normal breast tissue and invasive cancer. This is due to differences in collagen content between the two tissue types, with fibrous stroma being significantly more birefringent than invasive tumor. Additionally, the use of a high-speed imaging system and GPU processing allows for real-time PS-OCT imaging suitable for intraoperative applications. These results suggest that PS-OCT should be further developed for integration with current OCT efforts in breast cancer imaging, including both tumor margin and biopsy assessment.

Acknowledgments

This work was supported in part by grants from the National Institutes of Health (R01 EB012479, R01 CA166309, S.A.B.). The authors thank Dr. Partha Ray, Dr. Kimberly Cradock, and Dr. Magesh Sundaram for performing tissue resection, and Dr. Z. George Liu for histopathological evaluation. Special thanks to Adeel Ahmad and Nathan D. Shemonski for their helpful discussions. The authors also thank Professor James G. Fujimoto of the Massachusetts Institute of Technology for providing the FDML laser used in this study.